Constructing a Schottky junctions in PCL scaffolds: NIR triggers photo-electricity-catalysis coupling to promote osteogenic differentiation and antibacterial efficacy

Xiaohui Niu [a 1], Renjie Pan [c 1], Jiaxing Xiong [e], Xin Liao [f], Xuanyu Mao [a], Rongcheng Xu [a], Siyi Ye [f], Shanshan Cai [d 2], Hao Xing [b]

[a]Department of Trauma Orthopedics, Lishui Hospital of Wenzhou Medical University, The First Affiliated Hospital of Lishui University, Lishui People's Hospital, Lishui 323000, China

[b]Department of Rehabilitation Medicine, Shanxi Bethune Hospital, Shanxi Academy of Medical Sciences, Third Hospital of Shanxi Medical University, Tongji Shanxi Hospital, Taiyuan 030032, China

[c]Department of Laboratory Medicine, Xinghua People's Hospital Affiliated to Yangzhou University, Taizhou 225700, China

[d]Division of Biomedical and Life Sciences, Faculty of Health and Medicine, Lancaster University, Lancaster LA1 4YG, United Kingdom

[e]Faculty of Education, University Malaya, Kuala Lumpur 50603, Malaysia

[f]The First People's Hospital of Jiande, Hangzhou 311600, China

Corresponding authors. E-mail addresses: s.cai6@lancaster.ac.uk (S. Cai), xinghao@sxbqeh.com.cn (H. Xing). 1 These authors contribute equally 2 Shanshan Cai and Hao Xing are co-correspondences authors, with Hao Xing as the first

Abstract

Graphite-phase carbon nitride (g-C_3N_4) has attracted great attention in boosting the repair of infectious bone defects due to its extraordinary photoelectric conversion and carrier mobility. However, the excessive electron injection barrier and inefficient near-infrared (NIR) light absorption restrict its therapeutic efficacy. Herein, Cu nanoclusters (Cu NCs) were originally assembled on g-C_3N_4 by hydrothermal method, and interface defects were constructed to form Cu-g-C_3N_4 Schottky junctions, which were then added into polycaprolactone (PCL) scaffolds. On the one hand, Cu NCs induce surface electrons

collective oscillation to extend the light absorption into the NIR region, then the produced hot electrons migrate to the built-in electric field of g-C_3N_4 by the Schottky junction, thereby improving the photoelectric properties. On the other hand, Cu NCs can couple with π-conjugated structures to reduce electron injection barrier, and act as electron traps to enrich delocalized electrons, thus boosting electron-hole separation and photocatalysis efficiency. Results prove that the Cu-g-C_3N_4 exhibits excellent NIR absorption, and the enhancement of photoelectric effect can be proved by a 50 % increase in transient photocurrent. The electrical signal can boost osteogenic differentiation as evidenced by a 2.9-fold upregulation of ALP and ARS expression, and a 45 % increase in osteogenic differentiation-related mRNA and BMP-2 levels. ROS with a yield improved to 66.9 % can rapidly destroy biofilms to boost ROS entry into bacteria, causing protein leakage and GSH consumption, thus achieving antibacterial rates of 91.6 % and 92.4 % against *S. aureus* and *E. coli*, respectively.

1. Introduction

Infected bone defects (IBD), as a condition involving structural damage to bone tissue caused by surgery, trauma, or pathogenic bacterial invasion, are frequently accompanied by chronic inflammation and impaired bone regeneration, resulting in a significantly higher disability rate than non-infected bone injuries [1], [2]. Data indicates that the global treatment success rate for complex site infectious bone defects below 50 %, posing a severe threat to human health and life [3], [4]. Electrical stimulation therapy, leveraging its non-pharmacological regulatory advantages, can modulate intracellular signaling pathways and ion channel activity to promote the secretion of osteogenic factors such as osteomorphogens, thus creating a favorable microenvironment for bone regeneration [5], [6]. However, conventional electrical stimulation is constrained by external wires and invasive electrodes, which not only disrupt the bone tissue microenvironment but also heighten the risk of infection recurrence and hinder bone healing [7], [8]. Consequently, given the clinical challenges such as difficult infection control, low regeneration efficiency and invasive treatments, it is urgent to develop a safe, effective and non-invasive electrical stimulation bone regeneration strategy [5], [9].

Recently, wireless stimulation has garnered significant attention in the field of bone repair due to its wireless power supply, in-situ energy delivery, and controllable electrical signaling. Current research focuses on developing piezoelectric response electrical stimulation and triboelectric nanogenerators. For instance, Wu et al. designed an ultrasonically activated piezoelectric composite membrane capable of generating piezoelectric signals to modulate osteoblast and osteoclast generation, thus promoting osteogenic differentiation. Wang et al. constructed a wearable pulsed triboelectric nanogenerator that harnesses electrical signals generated from human movement deformation to boost angiogenesis, thus enhancing bone repair capabilities. However, the core principle of piezoelectric/triboelectric nanogenerators relies on mechanical deformation to produce electrical signals. Inadequate deformation during patient rest or unstable movement frequencies prevents the generation of sustained, uniform electrical signals, limiting their efficacy in bone defect repair applications.

Phototherapy has demonstrated irreplaceable value in bone tissue repair due to its non-invasive, spatiotemporal controllable and deep tissue penetration properties [10], [11]. Among numerous photoelectric materials, graphite-phase carbon nitride (g-C_3N_4) is considered one of the most promising candidate materials due to its advantageous photoelectric conversion, carrier mobility, and physicochemical stability [12], [13]. Besides, the internal electric field and electron traps formed between the "six-fold cavity" center and the band structure in g-C_3N_4 facilitate the transition of photogenerated charges to active sites, further reacting with O_2 to produce ROS for antibacterial, proving its application prospects in the treatment of infectious bone defects [14], [15]. For example, Liu et al. [16] developed a CuO/g-C_3N_4 thin film that exhibits a photocurrent density of $-2.27\ mA/cm^2$. Zhang et al. [17] constructed an antibacterial agent with efficient electron transfer based on RGO/g-C_3N_4, which showed excellent antibacterial activity against *E. coli* under illumination. Nevertheless, the excessive electron injection barrier and inefficient near-infrared light absorption severely restrict its application effectiveness [18], [19], [20].

In this study, Cu nanoclusters (Cu NCs) were anchored in-situ on g-C_3N_4 by hydrothermal method, forming a Cu-g-C_3N_4 Schottky junctions. Subsequently, it was added into a polycaprolactone (PCL) scaffold prepared by laser additive manufacturing, aiming to achieve

infectious bone defect repair (Fig. 1). On the one hand, Cu NCs can induce electrons collective oscillation to extend the light absorption to the near-infrared region, then the produced hot electrons migrate to the built-in electric field via the Schottky junction, enhancing the photoelectric effect. On the other hand, Cu NCs can introduce defect energy levels to weaken electron injection barrier, and act as electron traps to capture delocalized electrons, thus enhancing photocatalysis efficiency. The microstructure and physicochemical properties of the material were systematically analyzed, and the photoelectric and photocatalysis performance of the scaffold were thoroughly studied. The coupling enhancement mechanisms of photo-electricity-catalytic were identified by photoelectrochemical analysis. The promotion effect of scaffolds on cell osteogenic differentiation was explored by cell experimental, and the antibacterial properties and potential mechanism of scaffolds were comprehensively evaluated via antibacterial tests.

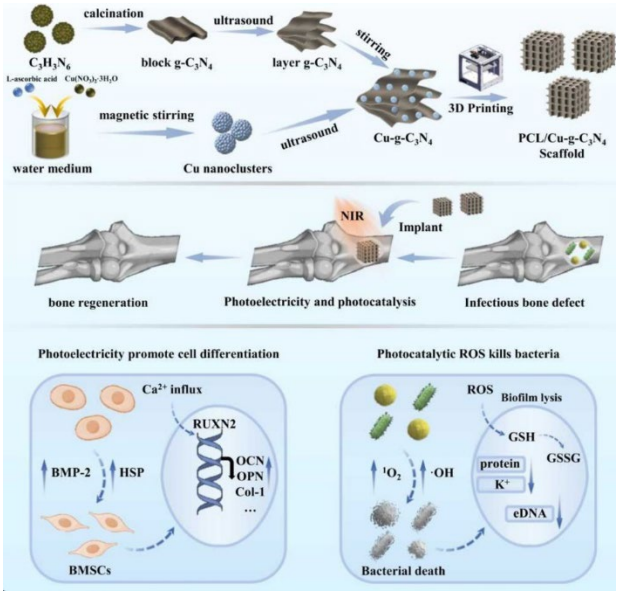

Fig. 1. (a) Schematic of PCL/Cu-g-C_3N_4 scaffold fabrication and (b) dual-pathway mechanism for infected bone repair via photoelectric stimulation and photocatalytic activation.

2. Materials and methods

2.1. Materials and reagents

Poly-ε-caprolactone (PCL) power was purchased from Guangzhou Chuangsai Biomedical Materials Co., Ltd. L-ascorbic acid (> 99.9 %), $Cu(NO_3)_2 \cdot 3\ H_2O$ (> 99.9 %), and melamine ($C_3H_6N_6$, > 99.9 %) were provided by Shanghai McLean Biochemical Technology Co., Ltd.

2.2. Preparation of Cu-g-C_3N_4 and scaffold

Graphite-phase carbon nitride (g-C_3N_4) was synthesized via thermal polymerization following established methodologies. Briefly, 10 g of melamine was subjected to calcination at 550°C for 6 h (heating rate: 10 °C/min) to produce bulk g-C_3N_4. Nanosheets were subsequently obtained through aqueous exfoliation, wherein 500 mg of bulk powder was dispersed in 200 mL deionized water and ultrasonicated for 24 h. The resulting suspension underwent centrifugation at 10,000 rpm to isolate exfoliated nanosheets. For copper modification, a colloidal copper nanocrystal (Cu NC) solution was first prepared by vigorously stirring L-ascorbic acid with $Cu(NO_3)_2 \cdot 3\ H_2O$ in aqueous medium at ambient temperature for 4 h, yielding a pale-yellow dispersion. This Cu NC solution was then combined with the g-C_3N_4 nanosheets, followed by 2 h of sonication and 2 h of magnetic stirring. The homogenized mixture was finally dried at 80°C for 24 h to obtain Cu-g-C_3N_4 composite.

Composite scaffolds were fabricated via laser additive manufacturing technique. Initially, PCL was blended with g-C_3N_4 or Cu-g-C_3N_4 powders, followed by drying and ball-milling to obtain homogeneous PCL/g-C_3N_4 and PCL/Cu-g-C_3N_4 composite feedstocks. Then, PCL/g-C_3N_4 and PCL/Cu-g-C_3N_4 scaffolds were constructed by selective laser sintering, with the following preparation conditions: (Ⅰ) powder deposition: composite powders were uniformly spread into thin layers (100μm layer thickness) using a precision roller; (Ⅱ) laser sintering: a fiber laser selectively fused powder layers at 8 W power with a scanning speed of 600 mm/s; (Ⅲ) hatching strategy: parallel scanning vectors were applied at 100μm hatch spacing to ensure structural continuity; (Ⅳ) atmosphere control: processing occurred under nitrogen atmosphere to prevent polymer oxidation; (Ⅴ) layer stacking: sequential powder deposition and sintering cycles built scaffolds layer-by-layer.

2.3. Materials characterization

The microstructure and elemental mapping of g-C_3N_4 and Cu-g-C_3N_4 were characterized

using transmission electron microscopy (TEM, JEM-ARM300F, JEOL Ltd, Japan) coupled with energy-dispersive spectroscopy (EDS, QUANTAX, Bruker, Germany). Crystalline phase identification was performed via X-ray diffraction (XRD, D8 ADVANCE, Bruker, Germany). Surface chemical states were analyzed by X-ray photoelectron spectroscopy (XPS, PHI 5000, ULVAC-PHI, Japan), while ultraviolet photoelectron spectroscopy (UPS, AXIS Supra+, Shimadzu-Kratos, Japan) determined the work function. UV-Vis-NIR spectrophotometers (Lambda 365, PerkinElmer, Singapore) are used to measure the light absorption properties of materials.

2.4. Photoelectric property detection of scaffold

Photoelectricity properties were assessed through electrochemical measurements (VSP-300, Bio-Logic Science Instruments, France) under the illumination of the set light source. Specifically, a standard three-electrode system was employed for all measurements, comprising: catalyst-coated indium-tin oxide (ITO, 1 cm^2) as the working electrode; Platinum wire counter electrode (Ø 0.5 mm, length 5 cm); Ag/AgCl (saturated KCl) reference electrode in 0.5 $mol \cdot L^{-1}$ Na_2SO_4 electrolyte. Measurements were executed at 10 mV bias in this consecutive sequence: cyclic voltammetry (50 $mV \cdot s^{-1}$ scan rate), linear sweep voltammetry (0–1.2 V vs. RHE), current density-voltage profiling, electrochemical impedance spectroscopy (0.001–0.1 Hz, 0.5 V bias) and transient photocurrent response. Amone, transient photocurrent used automated shutter-controlled irradiation cycles (20 s light/20 s dark) with 300 W xenon lamp (AM 1.5 G, 100 $mW \cdot cm^{-2}$). All procedures complied with ISO 17025 testing standards for electrochemical measurements.

2.5. Photocatalytic activity detection of scaffold

Firstly, the signal peak of ROS was detected using ESR to determine the type of ROS, as detailed in S1. The hydroxyl radical (·OH) and singlet oxygen ($^1O_2$) generated by the scaffolds were quantified via oxidative degradation of specific molecular probes- 1,3-diphenylisobenzofuran (DPBF) for $^1O_2$ and methylene blue (MB) for ·OH. These probes exhibit unique absorption peaks that proportionally decrease upon reaction with their respective ROS, enabling indirect ROS measurement under NIR irradiation. Prior to testing, scaffolds

from each experimental group were equilibrated in 1.5 mL of probe solution (20 mg/L MB/DPBF in phosphate-buffered saline, pH 7.0) via 1 h dark incubation to establish adsorption-desorption equilibrium. Following addition of 10 µL 30 % H_2O_2 as an oxidant enhancer, the systems were subjected to NIR illumination while being monitored by UV–visible spectroscopy. The evolution of ROS production was tracked by recording probe absorbance after 10 min of irradiation, with the degradation rates of MB (664 nm) and DPBF (410 nm) directly correlating to ·OH and $^1O_2$ generation capacities, respectively. This spectrophotometric approach provides a sensitive and quantitative test of scaffold photocatalytic activity via well-established probe decomposition kinetics under controlled experimental conditions.

2.6. Antibacterial experiment

The antimicrobial efficacy of scaffolds was quantitatively assessed through standardized colony counting. Prior to testing, scaffolds underwent sequential sterilization: immersion in 75 % ethanol followed by UV irradiation (3 h). Bacterial suspensions were cocultured with sterilized scaffolds at 37°C for 12 h, followed by 10 min light exposure (test group) or dark incubation (control). Post-treatment, cultures were diluted to 1×10^{12} CFU/mL, with 30 µL aliquots spread on LB agar plates. After 24 h incubation at 37°C, colony formation was documented photographically and quantified using ImageJ. Antibacterial rate (%) was calculated as:

$$\text{Antibacterial rate}(\%) = (\text{CFU}_{\text{control}} - \text{CFU}_{\text{treatment}})/\text{CFU}_{\text{control}} \times 100\%$$

where $CFU_{control}$ represents the bacterial count in untreated samples, while $CFU_{treatment}$ indicates the bacterial survival after scaffold exposure under both illuminated and non-illuminated conditions.

Bacterial morphology following treatment was examined via scanning electron microscopy (SEM). After 12 h co-culture with *S. aureus* or *E. coli* (37°C), scaffolds underwent either 808 nm NIR irradiation (10 min) or dark incubation. Fixed in 2.5 % glutaraldehyde (30 min) and dehydrated through an ethanol gradient (30–100 %), samples were gold-sputtered for

SEM imaging to evaluate bacterial adhesion and structural integrity. Subsequently, AM/PI probes were used to evaluate bacterial viability/death, with live bacteria emitting green fluorescence and dead bacteria emitting red fluorescence. Post-treatment bacterial suspensions were washed, centrifuged, and incubated with 150 μL probes (1 h, dark). Then, ImageJ software quantifies survival rate based on green/red emission ratio.

To evaluate biofilm permeability, crystal violet staining was performed, with detailed procedures provided in Supporting Information S2. Besides, intracellular ROS levels, biomolecule leakage, and glutathione (GSH) depletion were quantified to assess oxidative stress responses (methodological details in Supporting Information S3).

2.7. Cell behavior analysis

Bone marrow mesenchymal stem cells (BMSCs) were employed as an in vitro model to evaluate cellular responses to scaffold intervention. Cells (2×10^4/mL) were initially cultured in RPM-1640 medium containing horse serum (10 %),fetal bovine serum (10 %), penicillin (100 U/mL) and streptomycin (100 μg/mL) under standard conditions (37°C, 5 % CO_2). Following cell adhesion, sterilized scaffolds were introduced into the culture system. During the experimental period (duration adjusted per study objectives), samples received intermittent laser exposure (20 s ON/OFF cycles) administered every 24 h.

2.7.1. Cytotoxicity and proliferation

After co-culturing for 1 and 3 days, cell viability was evaluated using live/dead staining (Calcein-AM/PI). After scaffold removal, cells were detached using trypsin-EDTA, washed with PBS (×3), and stained for 1 h at 37°C before fluorescence microscopy. Additionally, the cell survival rate (viability) was calculated by previously reported formula [21], [22], [23]. After co-culturing for 1 and 3 days, cell proliferation was quantified via CCK-8 assay: cell-laden scaffolds were transferred to serum-free medium with 10 % CCK-8 solution, incubated for 1 h, and OD values measured at 450 nm.

2.7.2. Cell adhesion and F-actin labeling

Following 3-day co-culture, cell attachment was evaluated by SEM. Samples underwent

fixation (2.5 % glutaraldehyde, 1 h, RT) and ethanol gradient dehydration before imaging to assess cellular adhesion density and morphology. Following 3 days of co-culture, cells were gently washed with PBS to detach from scaffolds before undergoing 30 min of fixation and subsequent rinsing to eliminate fixative residues. The samples were then simultaneously stained with an F-actin probe (for cytoskeletal visualization) and DAPI (for nuclear labeling) for 1 h, followed by fluorescence microscopic examination to evaluate actin fiber organization, density and spatial distribution patterns.

2.7.3. Ca^{2+} influx and cell differentiation

During cellular differentiation, calcium ion (Ca^{2+}) influx was monitored using Fluo-4 AM staining, where cells were incubated with the fluorescent probe at 37°C for 30 min after 3 days of co-culture to ensure complete cellular uptake. Fluorescence microscopy captured the green emission signals, whose intensity variations directly correlated with intracellular Ca^{2+} concentration dynamics, followed by semi-quantitative analysis of fluorescence intensity using ImageJ software to evaluate calcium influx levels.

The osteogenic potential of scaffolds was evaluated through alkaline phosphatase (ALP) activity and calcium deposition analysis. After 14 days of co-culture, cells were stained with BCIP/NBT for ALP detection (30 min incubation) or Alizarin Red S (ARS) for calcium nodule visualization, followed by scaffold removal. Fluorescence microscopy revealed dark purple ALP staining indicating early osteogenic differentiation and pink ARS staining reflecting mineralized matrix formation. Both ALP and ARS staining intensities were quantified using ImageJ software to assess differentiation progression from early to late stages.

2.7.4. Protein and RT-qPCR analysis

After 5 days of scaffold co-culture, cells underwent immunostaining beginning with 5 % BSA blocking (12 h, 4°C) before sequential incubation with BMP-2 primary antibody and fluorescent secondary antibody, followed by nuclear counterstaining with DAPI. Fluorescence microscopy visualized green (BMP-2 expression) and blue (nuclear) signals, with quantitative analysis performed using ImageJ software to determine protein expression levels based on fluorescence intensity measurements. The detailed process of RT-qPCR analysis can be found

in Supporting Information S4.

2.8. Statistics

Quantitative results are presented as mean ± SD (standard deviation). Statistical significance between groups was determined by one-way ANOVA, with significance levels denoted as follows: $p < 0.001$ (***), $p < 0.01$ (**), and $p < 0.05$ (*).

3. Result and discussion

3.1. Characterization of Cu-g-C_3N_4

Firstly, the morphology and elemental distribution of Cu-g-C_3N_4 were characterized using transmission electron microscopy (TEM) and energy-dispersive X-ray spectroscopy (EDS). TEM imaging shows that g-C_3N_4 has a unique ultra large specific surface area and smooth surface morphology (Fig. 2a) [24]. Fig. 2b shows abundant Cu NCs deposited on the surface of g-C_3N_4, maximizing the utilization its surface structural advantages. Further observations of the microstructure of Cu NCs in g-C_3N_4 was conducted through HAADF-STEM (Fig. 2c). Fig. 2d shows the Fourier transform image in Fig. 2c, where 0.292 nm corresponds to the (100) crystal plane and 0.326 nm corresponds to the (002) crystal plane of g-C_3N_4 [25], [26]. The diffraction ring further confirmed the existence of crystal planes in Cu-g-C_3N_4 (Fig. 2e). Notably, the diffraction spots exhibited no regular features, which can be attributed to the crystalline order of the material, sample preparation quality, and testing conditions. The core reason is that after modifying pristine g-C_3N_4 with 1–10 nm Cu-NCs, the formation of Cu-N coordination bonds disrupts the long-range order of the g-C_3N_4 ring structure. Cu-NCs tend to be amorphous or low-crystalline, and their synergistic effect prevents the Cu-g-C_3N_4 composite from generating regular diffraction signals. Additionally, the EDS elemental map confirmed the uniform distribution of the main constituent elements, including carbon (C), nitrogen (N), oxygen (O) and copper (Cu) (Fig. 2f), and the mapping revealed the uniformly dispersed Cu nanoclusters throughout Cu-g-C_3N_4 [27].

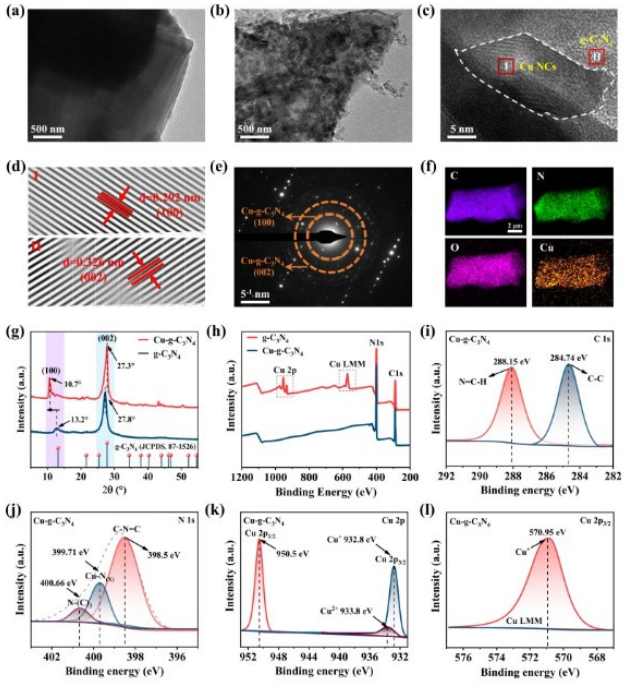

Fig. 2. (a) TEM image of g-C_3N_4; TEM (b), HRTEM (c), Fourier transform lattice (d) and diffraction ring images (e) of Cu-g-C_3N_4; (f) EDS element distribution of Cu-g-C_3N_4; XRD (g) and XPS spectra (h) of g-C_3N_4 and Cu-g-C_3N_4; XPS orbital peaks of (i) C 1 s, (j) N 1 s, (k) Cu 2p, and (l) Cu LMM in Cu-g-C_3N_4.

The unique crystallographic characteristics of g-C_3N_4 and Cu-g-C_3N_4 were revealed using XRD analysis (Fig. 2g). The pristine g-C_3N_4 showed characteristic reflections at 13.2° ((100) plane, corresponding to in-plane tri-s-triazine periodicity) and 27.8° ((002) plane, corresponding to π-stacked aromatic layers) [28]. In contrast, Cu NCs incorporation induced systematic peak displacements to 10.7° and 27.3°, consistent with lattice expansion from Cu nanocluster intercalation [29]. The intensified (100) reflection indicated Cu-mediated crystallite enlargement [30]. Crucially, no distinct diffraction peaks corresponding to copper oxides (CuO/Cu_2O), or Cu-C clusters were detected, indicating the absence of such crystalline phases. This suggests that Cu may exist in an amorphous state, possibly forming Cu-N coordination bonds with the tri-s-triazine motifs of g-C_3N_4 rather than aggregating into metallic or oxidized species [31], [32].

XPS was employed to characterize the elemental composition and chemical states of the

samples (Fig. 2h-l). Survey scan confirmed the presence of C, N, Cu, and surface-adsorbed O in Cu-g-C_3N_4, with the detection of Cu signal directly verifying the successful incorporation of Cu species (Fig. 2h). High-resolution C 1 s spectrum (Fig. 2i) exhibited two characteristic peaks at 284.74 eV (C-C bonds, edge graphitic carbon) and 288.15 eV (N = C-H bonds, sp^2-hybridized carbon in triazine rings) [33]. No peak shift was observed compared to pristine g-C_3N_4, indicating that Cu doping did not alter the carbon skeleton structure of g-C_3N_4 [34].

Detailed analysis of N 1 s spectrum (Fig. 2j) revealed conventional peaks at 398.5 eV (C-N = C bonds, bridging nitrogen) and 400.66 eV (N-$(C)_3$ bonds, edge amino defects), along with a new characteristic peak at 399.1 eV. This new peak was assigned to Cu-N coordination bonds (Cu-N(x) structure, tertiary amine nitrogen) formed by nitrogen atoms in the six-membered ring cavity of g-C_3N_4 donating lone pair electrons to Cu NCs, serving as direct evidence for chemical bonding between Cu and the triazine ring framework [35].

Cu 2p spectrum (Fig. 2k) displayed spin-orbit splitting peaks at 932.8 eV (Cu $2p_{3/2}$, corresponding to Cu^+) and 950.5 eV (Cu $2p_{1/2}$), with satellite peaks of Cu $2p_{3/2}$ indicating trace amounts of Cu^{2+} (surface oxidation products). Combined with the main peak at 570.05 eV in Cu LMM Auger spectrum (Fig. 2l, characteristic signal of Cu^+), these results proved that Cu in the composite primarily exists in Cu^+-N coordination structure, with no metallic Cu^0 or substantial oxidized Cu^{2+} detected [36]. This Cu-N coordination interaction significantly enhances the π-electron delocalization of g-C_3N_4 via electron transfer from N to Cu [37]. Concurrently, triazine ring units form interlayer extended conjugated systems, reducing the dissociation energy barrier of O_2 molecules at CuN_x sites and facilitating ROS generation [38].

Furthermore, XPS elemental analysis verified the coexistence of C, N and Cu in the Cu-g-C_3N_4 composite and provided crucial quantitative data for determining the Cu nanoclusters (Cu NCs)/g-C_3N_4 binding ratio. The atomic percentages of C, N and Cu were 58.2 %, 33.5 % and 8.3 %, respectively. Based on these data and g-C_3N_4's chemical composition (theoretical formula C_3N_4, C: N atomic ratio 3:4), the Cu NCs/g-C_3N_4 molar ratio was calculated as approximately 1:12 via molar conversion.

To further confirm the existence of Cu nanoclusters, FT-IR testing yielded results as shown

in Supporting Information Fig. S1. In the Cu-g-C_3N_4 composite material, the characteristic functional group absorption peak of g-C_3N_4 underwent significant changes, especially the N related vibration peak (1200–1600 cm^{-1} interval), which was caused by the formation of coordination bonds between Cu NCs and N atoms on the surface of g-C_3N_4, further confirming the existence of Cu NCs from the perspective of ligand interactions.

3.2. Photoelectric effect and enhancement mechanism of scaffold

Firstly, electron paramagnetic resonance (EPR) quantified delocalized electron density in the samples (Fig. 3a). Cu-g-C_3N_4 exhibited a sharp resonance at g= 2.00393, arising from unpaired π-electrons in tri-s-triazine rings [39]. Notably, its spin intensity was significantly higher than pristine g-C_3N_4, indicating more delocalized charge carriers [40]. This result stems from Cu-N coordination bonds, which donate electrons to extend π-conjugation in g-C_3N_4 [37], [41]. The enhanced delocalization improves electron transfer kinetics, creating an efficient charge transport pathway for catalysis.

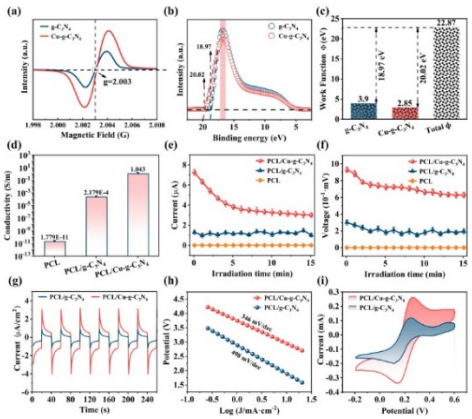

Fig. 3. Electron paramagnetic resonance (a) and work function (b, c) of g-C_3N_4 and Cu-g-C_3N_4; conductivity (d), output current (e) and output voltage (f) of PCL, PCL/g-C_3N_4 and PCL/Cu-g-C_3N_4; transient response photocurrent (g), Tafel fitting curve (h), cyclic voltammetry curve (i) of PCL/g-C_3N_4 and PCL/Cu-g-C_3N_4.

Then, Ultraviolet photoelectron spectroscopy was utilized to determine the work function (WF, Φ) of the samples, providing critical insights into interfacial charge migration

behavior [42], [43]. As depicted in Figs. 3b and 3c, Cu-g-C_3N_4 exhibits a reduced WF (Φ=2.85 eV) compared to pristine g-C_3N_4 (Φ = 3.9 eV). This downward shift in Φ indicates a lowered Fermi level, facilitating electron overflow from the valence band and enhancing electron-supply [44]. The decreased WF not only promotes interfacial electron transfer to adsorbed reactants but also strengthens the driving force for charge separation, collectively contributing to the observed enhancement in catalytic activity by optimized redox kinetics [45].

The output electrical signal, photoresponse and charge transfer properties of the scaffolds were systematically evaluated. Fig. 3d showed that the electrical conductivity of PCL/Cu-g-C_3N_4 (1.043 S/cm) was enhanced by 4 orders of magnitude compared to PCL/g-C_3N_4 ($\sim10^{-4}$ S/cm) and 11 orders of magnitude relative to PCL ($\sim10^{-11}$ S/cm), which could be ascribed to the Cu-N coordination-induced extension of π-conjugation in g-C_3N_4, facilitating efficient charge carrier transport via the conductive network [23]. As observed in Figs. 3e and 3f, PCL/Cu-g-C_3N_4 exhibited a stable output of current ($\sim$3 μA) and voltage ($\sim$0.6 mV). Although accompanied by attenuation (Voltage of about 30 % within 15 min), it's value significantly better than PCL/g-C_3N_4 ($\sim$1 μA, $\sim$0.25 mV) and PCL.

The transient photocurrent further validated the charge separation mechanism, and it was evident that the photocurrent generated by the PCL/Cu-g-C_3N_4 scaffold exceeded twice that of PCL/g-C_3N_4 (Fig. 3g), which was due to Cu-N coordination sites acting as electron traps, suppressing e^--h^+ recombination. The Tafel fitting line in Fig. 3h shows that the Tafel slope (346 mV/dec) of PCL/Cu-g-C_3N_4 is smaller than that of PCL/g-C_3N_4 (498 mV/dec), indicated accelerated reaction kinetics via delocalized π-electrons promoting O_2 activation. Cyclic voltammetry curve (Fig. 3i) proved superior charge storage in PCL/Cu-g-C_3N_4, with higher current density, redox potential and enhanced I-V loop rectangularity, reflecting efficient double-layer charge accumulation.

Further systematic analysis of the enhancement mechanism of Cu NCs doping on g-C_3N_4 photoelectric effect. Specifically, linear sweep voltammetry (Fig. 4a) showed enhanced redox peaks for PCL/Cu-g-C_3N_4 versus PCL/g-C_3N_4, while Nyquist plots (Fig. 4b) revealed smaller charge transfer resistance (reduced semicircle diameter), confirming Cu-N

coordination-mediated π-electron delocalization.

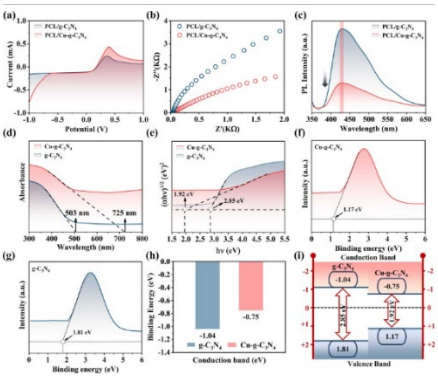

Fig. 4. Linear sweep voltammetry (a), Nyquist impedance spectra (b), and PL spectra (c) of PCL/g-C_3N_4 and PCL/Cu-g-C_3N_4; UV-Vis-NIR absorption spectra (d), bandgap (e), XPS valence band (f, g), and conduction band potential (h) of g-C_3N_4 and Cu-g-C_3N_4.

PL quenching (Fig. 4c) verified extended carrier lifetime in PCL/Cu-g-C_3N_4 via Cu-N electron trapping. The quenching of PL intensity in the PCL/Cu-g-C_3N_4 system is primarily attributed to a dual mechanism facilitated by Cu NCs for enhanced photogenerated carrier separation: On one hand, the formation of a Schottky junction between Cu NCs and g-C_3N_4 positions the Fermi level of Cu NCs below the conduction band minimum (CBM) of g-C_3N_4. This energy alignment drives the rapid transfer of photogenerated electrons to the Cu NCs surface, creating an "electron trap" that significantly suppresses e^--h^+ recombination. On the other hand, Cu-N coordination bonds enhance π-electron delocalization, establishing efficient charge transport pathways that further accelerate charge separation.

UV-Vis-NIR absorption spectra (Fig. 4d) displayed a redshift of the absorption edge from 503 nm (g-C_3N_4) to 725 nm (Cu-g-C_3N_4) with increased intensity, and Tauc plots (Fig. 4e) confirmed band gap narrowing (from 2.85 to 1.92 eV), expanding light absorption range and boosting e^--h^+ pair generation. Valence band spectrum shows that the valence band top (VB) of g-C_3N_4 is about 1.81 eV, while the VB of Cu-g-C_3N_4 drops to 1.17 eV (Figs. 4f and 4g). Combined with the conduction band bottom (CB) calculation (Fig. 4h, $E_{CB}=E_{VB}-E_g$), the CB of g-C_3N_4 is about −1.04 eV, and the CB of Cu-g-C_3N_4 rises to −0.75 eV, indicating that Cu NCs

doping adjusts the band structure. Band structure diagrams (Fig. 4i) summarized Cu doping effects: enhanced photoelectric performance arises from expanded light absorption/band gap narrowing (increased carrier generation) and reduced charge transfer resistance (improved charge transport).

3.3. Photocatalytic activity and enhancement mechanism of scaffold

To investigate the photocatalytic activity of the scaffold, ESR spectroscopy (Figs. 5a and 5d) was first used to detect the ROS production of PCL/Cu-g-C_3N_4 scaffold under NIR radiation [46]. Results showed that no characteristic signals were observed under dark conditions, but the addition of H_2O_2 and light induction resulted in clear free radical features. Specifically, the characteristic of DMPO/·OH adduct is a 1:2:2:1 quadruple (Fig. 5a), while the characteristic of TEMP/$^1O_2$ is a 1:1:1 triple (Fig. 5d) [47]. The above demonstrated that Cu NCs significantly enhance the photocatalytic ability to generate both ·OH and $^1O_2$ via improved light absorption and charge separation efficiency.

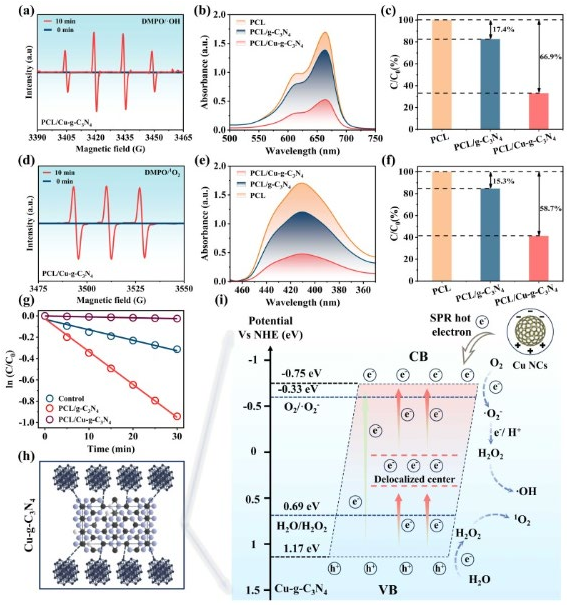

Fig. 5. ESR spectrum of ·OH (a) and $^1O_2$ (d) in PCL/Cu-g-C_3N_4; absorbance of MB (b) and DPBF (e) in PCL, PCL/g-C_3N_4 and PCL/Cu-g-C_3N_4; degradation rate of MB (c) and DPBF (f) in various scaffolds; (g) degradation kinetics curve of various scaffolds; Schematic diagram of the chemical state binding and photocatalytic enhancement mechanism of Cu-g-C_3N_4.

Meanwhile, photocatalytic ROS generation was quantified using MB (·OH probe) and DPBF ($^1O_2$ probe) [48], [49]. PCL/Cu-g-C_3N_4 showed higher MB and DPBF degradation than PCL/g-C_3N_4 and PCL in 15 min (Figs. 5c and 5e), attributed to enhanced charge separation and hole mobility. Subsequently, quantitative analysis confirmed the superior photocatalytic activity of Cu NCs-modified scaffolds (Figs. 5c and 5f). Specifically, during MB degradation, the degradation efficiency of pure PCL approaches 100 %, indicating no catalytic activity. Compared to PCL/g-C_3N_4 (C/C_o=17.4 %), the degradation efficiency of PCL/Cu-g-C_3N_4 increased by 49.5 % (C/C_o=66.9 %). This enhancement was attributed to Cu-N coordination-promoted π-electron delocalization and carrier separation, which accelerates substrate degradation rates [50]. For DPBF, PCL remained catalytically inactive, while PCL/Cu-g-C_3N_4 achieved a degradation efficiency of 58.7 %, representing a 43.4 % increase compared to PCL/g-C_3N_4 (C/C_o = 15.3 %).

First-order kinetic model fitting ($-\ln(C/C_0) = kt$, Fig. 5g) revealed a reaction rate constant k for PCL/Cu-g-C_3N_4 is 0.0309 min^{-1}, representing a 3.15-fold increase compared to PCL/g-C_3N_4 (0.0098 min^{-1}) [51], [52]. This kinetic optimization stems from the dual regulation of Cu NCs: the electronic de-saturation effect of Cu NCs narrows the bandgap to broaden light absorption, while the Cu-g-C_3N_4 Schottky barrier promotes charge separation, ultimately synergistically accelerating the generation of ·OH and $^1O_2$ [53], [54]. As illustrated in Figs. 5h and 5i, the downward shift of the VB enhanced the oxidation capacity of holes (facilitating the oxidation of H_2O to produce ·OH), while the upward shift of the CB increased the reduction capacity of electrons (facilitating the reduction of O_2 to produce ROS) [55], [56]. This synergistically promotes carrier separation and interfacial catalytic reactions.

The core objective of this study is to improve the photocatalytic performance of g-C_3N_4 by modifying it with copper clusters (Cu NCs). The experimental results showed that PCL/Cu-g-C_3N_4 increased the degradation efficiency of methylene blue (MB) by 49.5 % compared to PCL/g-C_3N_4. The core mechanism of this performance improvement is due to the π-electron delocalization effect caused by Cu-N coordination and the enhanced carrier separation efficiency. This catalytic system provides new ideas for the long-term treatment and clinical translation of bone scaffolds.

3.4. Cell behavior of scaffold

3.4.1. Cell adhesion and biocompatibility

SEM analysis revealed distinct cell adhesion behaviors of cells after 3 days of co-culture under NIR irradiation (Fig. 6a), with PCL scaffold showing poor cell attachment and limited pseudopodia extension compared to the enhanced cellular protrusions of PCL/g-C_3N_4. The PCL/Cu-g-C_3N_4 scaffold exhibit superior cell density, spreading and early osteogenic differentiation. Then, the biocompatibility of different scaffolds was evaluated via live-dead staining and CCK-8 assays after 1 day and 3 days of co-culture with BMSCs [57]. Fluorescence imaging reveals predominant green signals across all groups (Fig. 6b), indicating minimal cytotoxicity. Fig. 6c presents NIR-irradiated cell viability (normalized to PCL control), showing minimal differences among scaffolds after 1 day but progressive survival increases by day 3, with PCL/Cu-g-C_3N_4 proving exceptional viability (148.5 %). CCK-8 results (Fig. 6d) display similar OD values between groups at each timepoint but progressive increases over culture duration, confirming unaffected proliferation. These collective findings verify the excellent biocompatibility of PCL/Cu-g-C_3N_4. The PCL/Cu-g-C_3N_4 system shows increased cell viability/density from day 1 to day 3 with no obvious Cu toxicity, due to two key factors: (I) ultra-low Cu content (well below cytotoxic levels), Cu-g-C_3N_4 constitutes 3 % of the composite with a Cu/g-C_3N_4 molar ratio of 1:12, preventing toxic Cu ion release; (II) synergy of natural cell proliferation over 3 days and the NIR-responsive bioactivity of Cu-g-C_3N_4, which offers a more favorable microenvironment than PCL and PCL/g-C_3N_4.

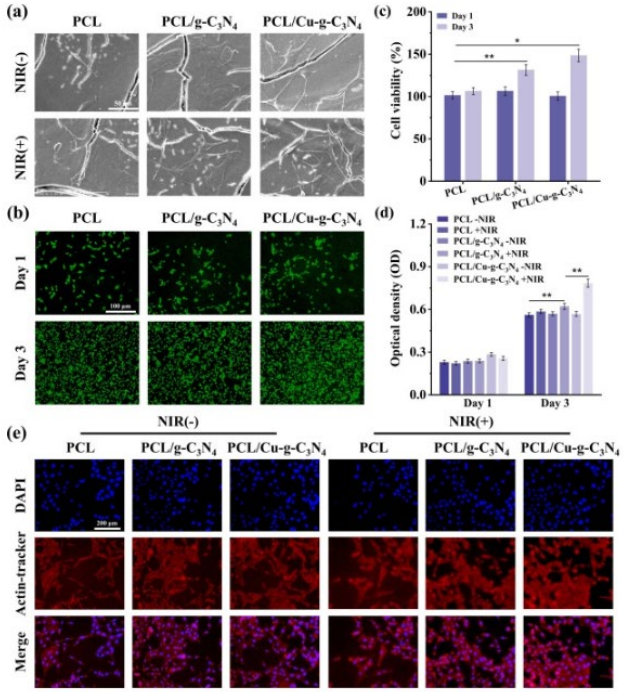

Fig. 6. (a) SEM images of cellular adhesion with or without NIR irradiation; live/dead staining analysis (b) and corresponding cell survival rate (c) after co-culture 1 and 3 days under NIR irradiation; (d) CCK-8 assays after co-culture 1 and 3 days in different scaffolds with or without NIR irradiation; (e) cytoskeletal organization staining via F-actin/nuclear co-staining after 3 days co-culture.

Comprehensive analysis of cytoskeleton structure using dual fluorescence staining after co-culture for 3 days, wherein rhodamine phalloidin specifically labeled F-actin filaments with red emission and DAPI counterstained nuclei with blue fluorescence. Detailed microscopic evaluation (Fig. 6e) proved progressively enhanced actin network organization across scaffold variants, revealing substantially improved filament integration and structural complexity in PCL/g-C_3N_4 composites compared to basic PCL controls. Most significantly, the PCL/Cu-g-C_3N_4 scaffold exhibited exceptional cytoskeletal development characterized by dense, well-aligned actin bundles and extensive cellular spreading morphology. This superior architectural organization persisted consistently under both near-infrared irradiated and non-irradiated experimental conditions, providing visual confirmation of the material's enhanced biocompatibility through robust cell-scaffold integration and favorable mechanobiological

interactions that support cellular health and function.

3.4.2. Cell differentiation and BMP-2 levels

Alkaline phosphatase (ALP) constitutes a critical early-stage biomarker for assessing osteogenic differentiation in BMSCs, with expression levels directly correlating to mineralization competence during osteogenic commitment [58]. Fig. 7a demonstrates substantially elevated ALP staining intensity in all NIR-exposed groups versus non-irradiated controls after co-culture for 14 days, confirming enzymatic activation requires NIR irradiation. Pure PCL exhibit negligible differentiation response under NIR, evidenced by minimal ALP staining, indicating inadequate photoelectrical performance. Conversely, NIR-irradiated PCL/g-C_3N_4 and PCL/Cu-g-C_3N_4 groups show significantly expand ALP-positive regions, with PCL/Cu-g-C_3N_4 displaying maximal intensity, indicating enhanced induction capacity. Quantitative analysis (Fig. 7b) validated these observations, proving that PCL/Cu-g-C_3N_4 exhibit higher staining intensity versus all groups at 14 days, establishing its superior osteogenic performance.

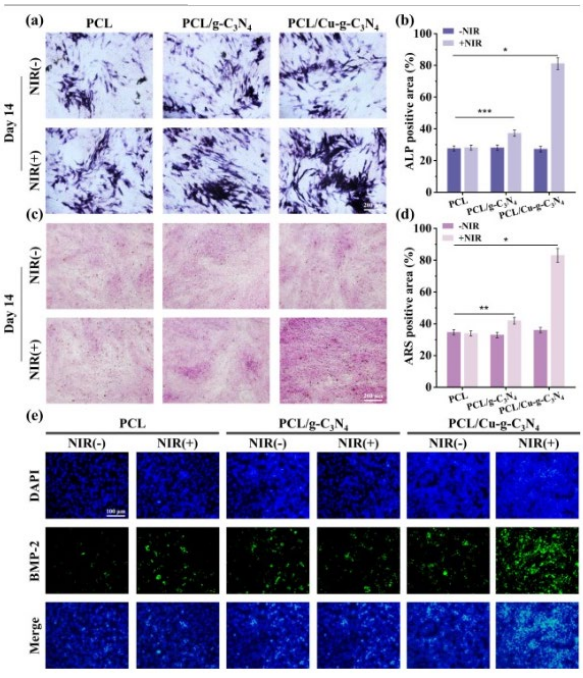

Fig. 7. (a) ALP expression following 14-day culture with or without NIR exposure, and (b) corresponding quantification; (e) mineralized matrix visualization via ARS staining, and (f) corresponding quantification at 14 days; (e) BMP-2 fluorescence staining after co-culturing

with each scaffold for 5 days.

Alizarin Red S (ARS) staining, a well-established histochemical technique that specifically binds to calcium-rich deposits and forms a bright red complex [59]. ARS staining at day 14 evaluated calcium deposition as a measure of late-stage osteogenic differentiation in BMSCs, with Fig. 7c showing comparably weak mineralization across non-irradiated groups. Following NIR application, the PCL and PCL/ g-C_3N_4 scaffold maintained minimal calcium nodule formation, confirming its photobiological inertness, while the PCL/Cu-g-C_3N_4 group demonstrate substantially enhanced mineralized nodule formation under identical irradiation conditions, indicating accelerated calcium accumulation. Complementary quantitative analysis of ARS staining intensity (Fig. 7d) provides conclusive evidence of PCL/Cu-g-C_3N_4 scaffold superior ability to promote advanced osteogenic maturation processes.

Bone morphogenetic protein-2 (BMP-2) functions as a core osteogenic regulator by activating Smad signaling to induce BMSC differentiation into osteoblasts while promoting bone matrix synthesis and mineralization [60]. Immunofluorescence analysis (Fig. 7e) reveals after 5 days of cultivation without NIR irradiation, the expression of BMP-2 on all scaffolds is weak and there is no significant difference between the groups. Following NIR exposure, PCL and PCL/g-C_3N_4 groups show unchanged fluorescence intensity, confirming their inability to stimulate BMP-2 expression. Notably, PCL/Cu-g-C_3N_4 group exhibits the most intense fluorescence with ubiquitous cellular distribution, indicating maximal photoelectricity enhancement of BMP-2 production through Cu-g-C_3N_4 synergy.

3.4.3. HSP70 and gene expression

HSP70 critically regulates cellular stress responses by maintaining protein folding integrity, suppressing apoptosis, and directly modulating BMSC osteogenic differentiation through upregulation of bone-related genes, serving as a key molecular indicator of differentiation progression [61]. As show in Fig. 8a, after co-culturing with the scaffold for 5 days, the green fluorescence of all experimental groups is very weak in a dark environment. Fig. 8b exhibit a

minimal HSP70 expression (green) in PCL group under NIR, whereas PCL/g-C_3N_4 show moderately increase fluorescence distribution. The PCL/Cu-g-C_3N_4 group exhibit near-complete cellular coverage by intense green signals, which is attributed to the electrophysiological microenvironment bring about by the photoelectricity generated by Cu-g-C_3N_4. The expression of HSP70 by photoelectric stimulation establishes a favorable intracellular environment for osteogenesis, confirming early ALP activity and calcium deposition results.

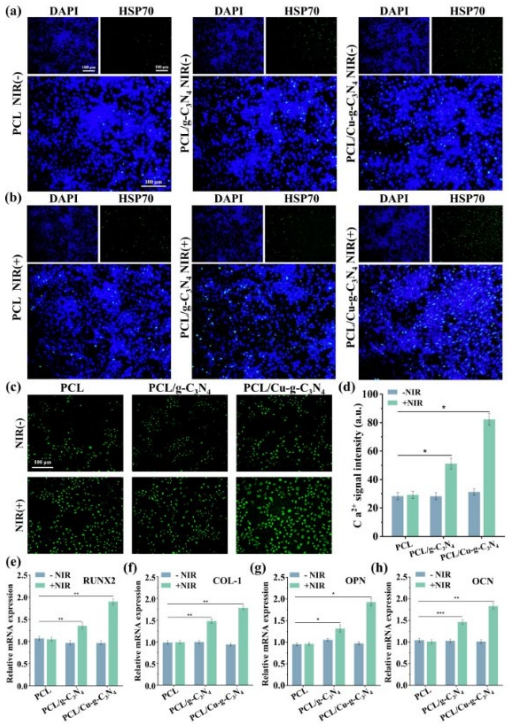

Fig. 8. Fluorescence staining under non NIR irradiation (a) and NIR irradiation (b) after co-culturing for 5 days; Ca^{2+} fluorescence staining (c) and corresponding quantitative results (d) after 3 days of cultivation; Relative mRNA expression of RUNX2, COL-1, OPN and OCN after 7 days of cultivation with or without NIR.

Intracellular Ca^{2+} serves as a crucial osteogenic signaling molecule, activating the Ca^{2+}/CaM/CaMKII pathway to regulate bone matrix synthesis and mineralization-related gene expression [62]. Fluo-4 fluorescence tracking revealed minimal Ca^{2+} levels in PCL and PCL/g-C_3N_4 scaffolds without NIR after 3 days of cultivation, while PCL/Cu-g-C_3N_4 exhibits

slightly higher baseline activity. NIR irradiation triggered dramatic Ca^{2+} influx in PCL/Cu-g-C_3N_4, evident through cell fluorescence (Figs. 8c and 8d), correlating with superior osteogenic performance in early differentiation markers, mineralization capacity, and genetic expression profiles compared to other groups.

The sequential activation of osteogenic genes forms the core molecular foundation governing BMSC differentiation dynamics, with RUNX2 functioning as the primary transcriptional activator initiating osteoblast lineage commitment during early differentiation, COL1 serving as the essential structural protein for bone matrix formation at intermediate stages, OPN acting as a mineralization process regulator coordinating calcium deposition, and OCN indicating terminal osteogenic maturation through direct reflection of bone mineralization completion. RT-qPCR analysis (Fig. 8e-h) proving that all relative mRNA expressions are upregulated in the PCL/g-C_3N_4 and PCL/Cu-g-C_3N_4 groups activated by NIR, compared to PCL. The strength of PCL/Cu-g-C_3N_4 reach a maximum of around 1.9. However, all experimental groups show a weak expression intensity of around 1.0 in dark condition.

Therefore, the photoelectric effect generated by PCL/Cu-g-C_3N_4 may promote Ca^{2+} influx, activate CaMKII/CREB signaling and epigenetic modification, synergistically amplify the BMP/Smad and Wnt/β-catenin pathways, explaining its superior bone induction at all differentiation stages [63], [64].

3.5. Antibacterial properties of scaffold

3.5.1. Antibacterial activity

Antibacterial efficacy of various scaffolds was quantitatively assessed via agar plate colony counting using *E. coli* and *S. aureus* models, with Fig. 9a revealing negligible bactericidal activity in dark conditions across all groups, confirming light-dependent ROS generation is essential for activation. Under NIR irradiation, PCL controls show minimal colony reduction, while PCL/g-C_3N_4 group exhibits moderate antibacterial effects attribute to limited ROS production. Differently, PCL/Cu-g-C_3N_4 can achieve massive bacterial eradication (<9 % residual colonies) through enhancing photocatalytic environmental oxygen generation of ROS. Quantitative antibacterial rates further prove the superior photocatalytic performance

of PCL/Cu-g-C_3N_4, exhibiting 91.6 % and 92.4 % inhibition against *S. aureus* and *E. coli* respectively, conclusively establishing its exceptional antibacterial properties.

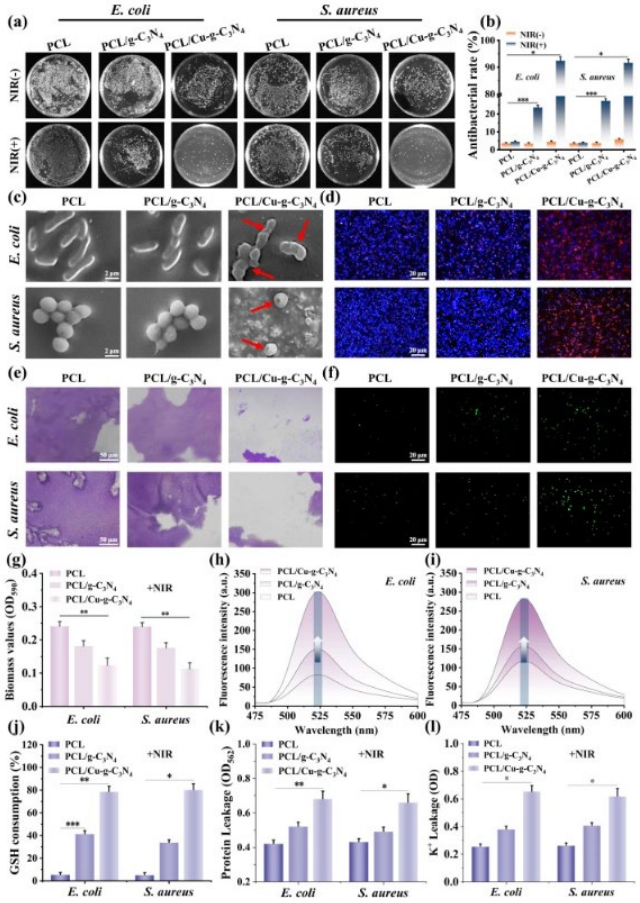

Fig. 9. The digital images of colonies after *E. coli* and *S. aureus* treated by scaffold (a), and the corresponding antibacterial rate (b); SEM images (c) and viability staining (d) of *E. coli* and *S. aureus* on the scaffold under NIR irradiation; Crystal violet staining (e) and corresponding quantitative results (g) under NIR irradiation; DCF fluorescence (f) and corresponding signal strength (h, i) in bacteria under NIR irradiation; GSH consumption (j), protein loss (k), and K^+ leakage (l) of bacteria in scaffolds.

Subsequently, SEM analysis of bacterial morphology further demonstrates the antibacterial efficacy of PCL/Cu-g-C_3N_4 scaffolds under NIR irradiation. Results revealing intact elongated *E. coli* and spherical *S. aureus* adhering to material surfaces in the PCL (Fig. 9c). Although NIR-exposed PCL group maintain normal bacterial morphology, PCL/g-C_3N_4 exhibit membrane folding in both bacterial. Strikingly, PCL/Cu-g-C_3N_4 group under identical illumination induced

severe cellular damage characterized by membrane rupture and structural collapse, confirming its unique capacity for bacterial structural destruction through photocatalytic mechanisms.

Membrane integrity assessment via PI/DAPI co-staining revealed PI selectively labels compromised membranes (red) while DAPI universally stains nuclei (blue), with Fig. 9d display minimal apoptotic signals in illuminated PCL group versus substantially increased PI fluorescence in PCL/g-C_3N_4. Notably, PCL/Cu-g-C_3N_4 exhibit intense PI penetration across both *E. coli* and *S. aureus* populations, confirming superior membrane disruption capacity attributable to photocatalytic copper clusters degrading biofilm barriers and facilitating ROS influx, thus establishing its mechanism for inducing irreversible photocatalytic impairment via targeted oxidative damage.

3.5.2. Antibacterial mechanism

To further explore the antibacterial mechanism of the scaffold, the integrity of the biofilm was first evaluated using crystal violet staining, as show in Fig. 9e. Under NIR irradiation, results reveal negligible biofilm disruption in PCL (dense purple coverage) versus partial biofilm degradation in PCL/g-C_3N_4 due to limited ROS generation ability. Remarkably, PCL/Cu-g-C_3N_4 exhibit near-complete biofilm elimination attribute to the enhancement of photocatalytic potency by Cu NCs. Furthermore, quantitative biomass confirms that the maximal biofilm accumulation of PCL, the larger biomass of PCL/g-C_3N_4, and the minimal biomass of PCL/Cu-g-C_3N_4 (Fig. 9g).

Subsequently, DCFH-DA fluorescence probing quantitatively measured bacterial ROS levels through oxidation-triggered green fluorescence emission (intensity proportional to ROS concentration). Fig. 9f displays negligible signals in PCL group versus moderate enhancement in PCL/g-C_3N_4 due to limited photocatalytic ROS generation under NIR illuminated. Interestingly, PCL/Cu-g-C_3N_4 group exhibit intense fluorescence, confirming maximal ROS production. DCF fluorescence intensity quantification shows markedly elevated intracellular signals in PCL/Cu-g-C_3N_4 treated bacteria post 10 min irradiation (Figs. 9h and 9i), confirming efficient ROS internalization via Cu NCs enhanced photocatalytic delivery mechanisms. These

603 results are attribute to the enhanced catalytic activity of Cu NCs, while damaging the
604 integrity of the membrane, thereby promoting the influx of large amounts of ROS
605 demonstrated by this photodynamic amplification cascade.

606 ROS incursion compromises bacterial antioxidant defenses, necessitating evaluation of
607 intracellular GSH depletion and biomolecule leakage. Fig. 9j demonstrates negligible GSH loss
608 in PCL group versus limit clearance in PCL/g-C_3N_4, while PCL/Cu-g-C_3N_4 group around 80 %
609 GSH depletion in both bacterial under NIR irradiation. Protein leakage assays reveal
610 substantial cytoplasmic efflux under NIR in PCL/Cu-g-C_3N_4 compared to other groups, the
611 leakage intensity in *E. coli* and *S. aureus* can reach 0.7 (Fig. 9k). Then, the loss rate of
612 K^+ affecting bacterial respiration was evaluated (Fig. 9l). Specifically, sodium
613 tetraphenylborate was used to detect the leakage intensity of K^+ under NIR radiation.
614 Obviously, the PCL/Cu-g-C_3N_4 group significantly exceeding the marginal leakage of PCL/g-
615 C_3N_4, proving that Cu NCs enhanced photocatalysis potentiates bacteriolytic capacity via
616 coordinate ion dysregulation and accelerate metabolic collapse.

617

618 **4. Conclusion**

619 In this work, Cu nanoclusters (Cu NCs) were assembled in-situ on g-C_3N_4 to form Cu-g-
620 C_3N_4 Schottky junctions via hydrothermal synthesis, followed by preparation of PCL/Cu-g-
621 C_3N_4 scaffold. On the one hand, Cu NCs induce collective electron oscillations extending light
622 absorption into the NIR region, then the generated hot electrons are efficiently transferred
623 to g-C_3N_4 via the Schottky junction, leveraging its built-in electric field to enhance
624 photoelectric activity. On the other hand, Cu NCs interact with π-conjugated structures in g-
625 C_3N_4 to weaken electron injection barrier, and simultaneously serve as electron traps to
626 accumulate delocalized electrons, thus optimizing overall photocatalysis efficiency. Results
627 prove that the scaffold exhibits excellent NIR absorption and sustained photoresponsive
628 wireless current. The electrical signal can boost osteogenic differentiation as evidenced by a
629 2.9-fold upregulation of ALP and ARS expression, and a 45 % increase in osteogenic
630 differentiation-related mRNA and BMP-2 levels. NIR activated scaffolds can rapidly lyse

biofilms to promote ROS entry into bacteria, reduce oxidative stress defense to accelerate bacterial death, thereby achieve antibacterial rates of 91.6 % and 92.4 % against *S. aureus* and *E. coli*, respectively. This study provides innovative strategies for the development of light activated electricity-catalysis integrated bone implants. This work achieves integrated osteogenesis and antibacterial therapy by coupling photo-electro-catalytic effects, providing novel insights into the clinical treatment of infected bone defects.

Authorship contribution statement

Jiaxing Xiong: Resources, Methodology, Investigation. Rongcheng Xu: Visualization, Validation. Siyi Ye: Validation, Supervision. Xin Liao: Software, Resources, Funding acquisition. Xuanyu Mao: Supervision, Software. Shanshan Cai: Visualization, Validation, Software, Resources, Methodology, Conceptualization. Hao Xing: Writing – review & editing, Funding acquisition, Formal analysis. Xiaohui Niu: Writing – original draft, Data curation, Conceptualization. Renjie Pan: Visualization, Validation, Investigation, Formal analysis.

Declaration of Competing Interest

The authors declare that they have no known competing financial interests or personal relationships that could have appeared to influence the work reported in this paper.

Acknowledgments

This study was supported by the following funds: (1) The basic research project of Shanxi Science and Technology Department (202403021222396); (2) Hangzhou Medical Health Science and Technology Plan Project (B20251637, B20220091); (3) Jiande Medicine Health Science and Technology Plan Project (2024SJZX08).

Supporting Information

S1. ESR analysis

To unequivocally identify the reactive species generated during photocatalysis, electron spin resonance (ESR) spectroscopy was employed using 2,2,6,6-tetramethylpiperidine (TEMP) as a singlet oxygen ($^1O_2$) trap and 5,5-dimethyl-1-pyrroline N-oxide (DMPO) as a hydroxyl radical (·OH) spin-trapping agent. Measurements were conducted using a Bruker EMXplus X-band spectrometer (9.85 GHz, 100 kHz modulation frequency) under controlled experimental conditions (microwave power: 10 mW, modulation amplitude: 1.0 G, temperature: 298 K).

For $^1O_2$ detection, scaffolds were dispersed in an aqueous solution containing 100 mM TEMP, and ESR spectra were recorded before and during 660 nm LED irradiation (100 mW/cm^2). The characteristic 1:1:1 triplet signal (a^N = 16.5 G, g = 2.006) confirmed $^1O_2$ generation. For ·OH detection, samples were sonicated in 50 mM DMPO solution, and ESR spectra were acquired under dark and 532 nm laser illumination (50 mW/cm^2). The distinctive 1:2:2:1 quartet signal ($a^N = a_H$ = 14.9 G, g = 2.006) verified ·OH formation. This ESR analysis quantitatively demonstrated the light-dependent generation of $^1O_2$ and ·OH, providing mechanistic insights into the photocatalytic ROS production pathways.

S2. Biofilm permeability

The crystal violet staining method is used to determine the survival rate of the biofilm after the action of the scaffold. Specifically, after 10 min of NIR irradiation, the scaffold is removed from the well plate and the plate is gently rinsed three times with PBS to remove the residual culture medium. Then, 200 μL of crystal violet solution was added and the plate was stained at 37 °C for 1 h. After washing with PBS and allowing to air dry naturally, observe the distribution of purple areas under a fluorescence microscope. Meanwhile, use a multifunctional microplate reader for quantitative analysis of the stained bacterial solution.

S3. Detection of intracellular ROS, biomolecule leakage and GSH consumption

Intracellular reactive oxygen species (ROS) were detected using the fluorescent probe 2',7'-dichlorodihydrofluorescein diacetate (DCFH-DA). Bacterial suspensions were co-incubated with the scaffolds for 24 h, followed by 10 min of near-infrared (NIR) irradiation or dark

control treatment. After removing the scaffolds, bacterial cells were washed, centrifuged, and stained with 300 μL DCFH-DA at 37°C for 1 h. Intracellular ROS accumulation was visualized via green fluorescence imaging using a fluorescence microscope, and DCF fluorescence intensity (λ_{ex}=488 nm, λ_{em}=525 nm) was quantitatively analyzed using a microplate reader to assess ROS generation levels.

Protein leakage and potassium ion (K^+) efflux assays were performed to evaluate bacterial membrane damage. For protein quantification, 25 μL of centrifuged bacterial supernatants (after scaffold co-incubation) was mixed with 100 μL Coomassie Brilliant Blue G250 reagent, incubated in the dark at 37 °C for 30 min, and absorbance was measured at 562 nm using a microplate reader. Parallel K^+ leakage analysis was conducted following the same supernatant collection protocol, with ion concentration quantified via flame atomic absorption spectroscopy (FAAS) or ion-selective electrode (ISE) to assess membrane permeability changes.

Glutathione (GSH) depletion capacity was evaluated using 5,5'-dithiobis(2-nitrobenzoic acid) (DTNB) as a colorimetric probe. Scaffolds were incubated with reduced GSH in the dark at 37 °C for 1 h, followed by 10 min of NIR irradiation (or dark control). The reaction mixture was then supplemented with 300 μL Tris-HCl buffer (pH 8.5) and 150 μL DTNB solution (500 mg/L), and absorbance was measured at 420 nm using a microplate reader after thorough mixing. GSH consumption efficiency was calculated using the formula:

GSH loss rate (%) = (1- $\frac{\mathrm{Anegative}}{\mathrm{Ascaffold}}$)/100%

where $A_{\mathrm{sample}}$and A_{control}represent absorbance values of NIR-irradiated and non-irradiated groups, respectively.

S4. RT-qPCR analysis

On day 5 of co-culture, total RNA was extracted following the Easy Total RNA assay protocol, with concentration measured using a B-500 biophotometer. The extracted RNA underwent reverse transcription after mixing with All-In-One RT-qPCR Mix, ds-DNase and nuclease-free water, followed by cDNA synthesis via PCR instrumentation. Following centrifugation and

defoaming to prepare the qPCR reaction solution, amplification cycles were performed on a sealed PCR plate to determine relative expression levels of osteogenesis-related marker genes through quantitative analysis.

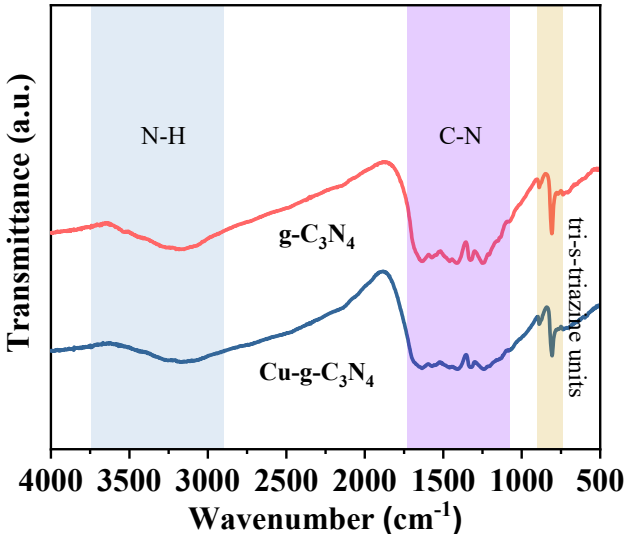

Fig. S1. FT-IR test results of g-C_3N_4 and Cu-g-C_3N_4 nanoparticles.

References

[1] J. Tang, J. Hu, X. Bai, Y. Wang, J. Cai, Z. Zhang, B. Geng, D. Pan, L. Shen, Nearinfrared carbon dots with antibacterial and osteogenic activities for sonodynamic therapy of infected bone defects, Small 20 (49) (2024) 2404900.

[2] J. Du, Y. Chu, Y. Hu, J. Liu, H. Liu, H. Wang, C. Yang, Z. Wang, A. Yu, J. Ran, A multifunctional self-reinforced injectable hydrogel for enhancing repair of infected bone defects by simultaneously targeting macrophages, bacteria, and bone marrow stromal cells, Acta Biomater. 189 (2024) 232–253.

[3] W.J. Metsemakers, T.F. Moriarty, M. Morgenstern, L. Marais, J. Onsea, R. V. O'Toole, M. Depypere, W.T. Obremskey, M.H. Verhofstad, M. McNally, The global burden of fracture-related infection: can we do better? Lancet Infect. Dis. 24

(6) (2024) e386–e393.

[4] N. Yan, H. Zhou, P. Jin, T. Li, Q. Liu, H. Ning, Z. Ma, L. Feng, T. Jin, Y. Deng, A Multifunctional cobalt-containing implant for treating biofilm infections and promoting osteointegration in infected bone defects through macrophage-mediated immunomodulation, Adv. Sci. 12 (3) (2025) 2409200.

[5] J. Sun, W. Xie, Y. Wu, Z. Li, Y. Li, Accelerated bone healing via electrical stimulation, Adv. Sci. 12 (24) (2025) 2404190.

[6] T. Wang, H. Ouyang, Y. Luo, J. Xue, E. Wang, L. Zhang, Z. Zhou, Z. Liu, X. Li, S. Tan, Rehabilitation exercise-driven symbiotic electrical stimulation system accelerating bone regeneration, Sci. Adv. 10 (1) (2024) eadi6799.

[7] K. Chen, B. Wu, D. Krahe, A. Vazquez, J.R. Siegenthaler, R. Rechenberg, W. Li, X. T. Cui, T.D. Kozai, Potential of photoelectric stimulation with ultrasmall carbon electrode on neural tissue: new directions in neurostimulation technology development, Adv. Funct. Mater. 34 (41) (2024) 2403164.

[8] Y. Huang, K. Yao, Q. Zhang, X. Huang, Z. Chen, Y. Zhou, X. Yu, Bioelectronics for electrical stimulation: materials, devices and biomedical applications, Chem. Soc. Rev. 15 (11) (2024) 2403175.

[9] Y. Yao, X. Cui, S. Ding, K. Wang, M. Zhang, Advances in electrical materials for bone and cartilage regeneration: developments, challenges, and perspectives, Adv. Sci. (2025) 2411209.

[10] D. Xu, X. Wang, M. Li, L. Xie, K. Liu, Y. Liu, J. Lan, P. Han, H. Lin, L. Song, Enhancing titanium-osteointegration: antimicrobial, anti-inflammatory and

750 osteogenic properties of multifunctional coatings through layer-by-layer selfassembly, Appl.
751 Surf. Sci. 686 (2025) 162149.
752 [11] M. Xie, T. Gong, Y. Wang, Z. Li, M. Lu, Y. Luo, L. Min, C. Tu, X. Zhang, Q. Zeng,
753 Advancements in photothermal therapy using near-infrared light for bone tumors,
754 Int. J. Mol. Sci. 25 (8) (2024) 4139.
755 [12] X. Yang, J. Peng, L. Zhao, H. Zhang, J. Li, P. Yu, Y. Fan, J. Wang, H. Liu, S. Dou,
756 Insights on advanced g-C3N4 in energy storage: applications, challenges, and
757 future, Carbon Energy 6 (4) (2024) e490.
758 [13] J. Pei, H. Li, D. Yu, D. Zhang, g-C3N4-based heterojunction for enhanced
759 photocatalytic performance: a review of fabrications, applications, and
760 perspectives, Catalysts 14 (11) (2024) 825.
761 [14] B. Zhang, S. Xia, Z. Wang, W. Li, B. Li, H. Zhang, Y. Xin, K. Wu, J. Ma, X. He,
762 Enhanced permanganate activation by g-C3N4 under visible light irradiation:
763 unraveled mechanism involving Mn (V) and photo-induced electron, Appl. Catal. B
764 Environ. Energy 349 (2024) 123861.
765 [15] G. Wu, Q. Wang, Q. Ren, Z. Mo, H. Xu, Molecular structure engineering of graphitic
766 carbon nitride for photocatalytic hydrogen evolution: recent advances and
767 perspectives, Small 22 (18) (2025) 2503954.
768 [16] D. Liu, M. Xiao, S. Jiang, J. Bai, R. Tao, Z. Chu, X. Fan, Y. Han, Fabricating CuO/gC3N4 films
769 to elucidate the critical role of surface state regulation in enhancing
770 photocathode performance, Appl. Surf. Sci. 692 (2025) 162687.
771 [17] J. Zhang, W. Wang, S. Huang, Y. Lv, M. Li, M. Wu, H. Wang, Metal-free
772 photocatalyst with reduced graphene oxide-doped graphitic carbon nitride

773 homojunctions for efficient antibacterial applications, RSC Adv. 15 (4) (2025)
774 2444–2451.
775 [18] M. Gao, M. Zhao, Q. Yang, L. Bao, L. Chen, W. Liu, J. Feng, A review on pre-, inprocess,
776 and post-synthetic strategies to break the surface area barrier in g-C3N4 for
777 energy conversion and environmental remediation, Nanomaterials 15 (13) (2025)
778 956.
779 [19] F. Zhou, W. Li, J. Wu, W. Yang, Y. Sun, H. Zhou, T. Jia, Y. Ling, P. He, W. Pan,
780 Enhanced solar-driven CO2 conversion: the role of Yb-doped CuInS2 quantum dots
781 on g-C3N4 nanosheets, Appl. Catal. B Environ. Energy 362 (2025) 124716.
782 [20] S. Deng, W.P. Xiong, G.X. Zhang, G.F. Wang, Y.X. Chen, W.J. Xiao, Q.K. Shi,
783 A. Chen, H.Y. Kang, M. Cheng, Metal-free modification overcomes the
784 photocatalytic limitations of graphitic carbon nitride: efficient production and in
785 situ application of hydrogen peroxide, Adv. Energy Mater. 14 (39) (2024)
786 2401768.
787 [21] Y. Wang, T. Chu, T. Jin, S. Xu, C. Zheng, J. Huang, S. Li, L. Wu, J. Shen, X. Cai,
788 Cascade reactions catalyzed by gold hybrid nanoparticles generate CO gas against
789 periodontitis in diabetes, Adv. Sci. 11 (24) (2024) 2308587.
790 [22] Y. Cai, M. Prochazkova, Y.-S. Kim, C. Jiang, J. Ma, L. Moses, K. Martin, V. Pham,
791 N. Zhang, S.L. Highfill, Assessment and comparison of viability assays for cellular
792 products, Cytotherapy 26 (2) (2024) 201–209.
793 [23] H. Li, X. Shuai, Y. Chen, J. Xiong, Z. Zou, S. Peng, F. Qi, C. Shuai, Engineering a
794 wirelessly self-powered neural scaffold based on primary battery principle to

accelerate nerve cell differentiation, Colloids Surf. B Biointerfaces 249 (2025) 114521.

[24] X. Zhang, S. Chen, F. Guo, Q. Jing, P. Huo, L. Feng, F. Sun, S. Chandrasekar, L. Hao, B. Liu, A novel method for synthesizing specific surface area modulable g-C3N4 photocatalyst with maize-like structure, Appl. Surf. Sci. 651 (2024) 159224.

[25] B. Zhao, D. Gao, W. Zhong, F. Chen, P. Wang, X. Wang, H. Yu, Highly intra-and inter-plane crystalline ReSx/g-C3N4: facile synthesis and boosted photocatalytic H2 evolution, Chem. Eng. J. 479 (2024) 147711.

[26] W. Zhong, D. Zheng, Y. Ou, A. Meng, Y. Su, Simultaneously improving inter-plane crystallization and incorporating K atoms in g-C3N4 photocatalyst for highlyefficient H2O2 photosynthesis, Acta Phys. Chim. Sin. 40 (11) (2024) 2406005.

[27] H. Islam, B. Jaksani, A. Iqbal, S. Varangane, H.V. Annadata, B. Ghosh, B.B. Sarma, R. Thapa, U. Pal, Atomically dispersed Cu–Ni dual-metal sites on g-C3N4 for synergistic enhancement of photocatalytic hydrogen evolution, ACS Appl. Energy Mater. 14 (35) (2025) 20254438.

[28] J. Nie, S. Yue, B. Li, J. Guo, C. Wu, Boosting piezo-catalytic H2 production on gC3N4 via carbon-ring doping to shorten in-plane charge transfer distance, Ceram. Int. 16 (11) (2025) 20256127.

[29] S. Biswas, Y. Negishi, A comprehensive analysis of luminescent crystallized Cu nanoclusters, J. Phys. Chem. Lett. 15 (4) (2024) 947–958.

[30] X. Xu, Y. Zhong, M. Wajrak, T. Bhatelia, S.P. Jiang, Z. Shao, Grain boundary engineering: an emerging pathway toward efficient electrocatalysis, InfoMat 6 (8) (2024) e12608.

[31] J. Huang, K. Geng, Y. Sun, Y. Wei, H. Hou, Electron localization engineering to construct Cu single-atom bridges between g-C3N4 layers for regulating third-order nonlinear optical properties, Nano Today 65 (2025) 102836.

[32] J. Qiu, D. Wang, Y. Chang, Q. Feng, Z. Liu, M. Pang, D. Meng, Y. Feng, C. Fan, Anchoring single-atom Cu on tubular g-C3N4 with defect engineering for enhanced Fenton-like reactions to efficiently degrade carbamazepine: performance and mechanism, Chem. Eng. J. 479 (2024) 147841.

[33] W.T. Chen, H.W. Shiu, Y.X. Chen, E. Batsaikhan, Y.L. Lai, S.L. Cheng, T. Araki, J. F. Lee, M. Hayashi, Y.J. Hsu, Highly selective toward HER or CO2RR by regulating Cu single and dual atoms on g-C3N4, Adv. Funct. Mater. 18 (35) (2025) e14183.

[34] S. Dwivedi, G. Pandey, Synergistic photocatalytic performance of MoO3: Cu/gC3N4 heterojunction semiconductor for efficient crystal violet dye degradation: a sustainable approach for environmental remediation, J. Mol. Struct. 1318 (2024) 139386.

[35] W. Zhang, M. Chen, Y. Luo, Y. He, S. Liu, Y. Ye, M. Wang, Y. Chen, K. Zhu, H. Shu, Utilizing 2D layered structure Cu-g-C3N4 electrocatalyst for optimizing polysulfide conversion in wide-temperature Li-S batteries, Chem. Eng. J. 486 (2024) 150411.

[36] S.P. Chenakin, N. Kruse, Surface composition and electronic properties of Co-Cu mixed oxalates: A detailed XPS analysis, Appl. Surf. Sci. 669 (2024) 160460.

[37] C. Ding, L. Yang, X. Lu, H. Chi, Y. Yang, J. Yuan, X. Wang, X. Wu, Y. Zhang, Y. Zhou, Outstanding CO2 photoreduction in single-atom thulium modified carbon nitride, Adv. Sci. 11 (38) (2024) 2406329.

[38] M. Shao, Y. Shao, H. Pan, Progress on enhancing the charge separation efficiency of carbon nitride for robust photocatalytic H2 production, Phys. Chem. Chem. Phys. 26 (15) (2024) 11243–11262.

[39] F. Attar, H. Yin, S.L. Schumann, J. Langley, N. Cox, Z. Zeng, K. Catchpole, S. Karuturi, Z. Yin, Advanced electron paramagnetic resonance in chemical energy conversion: current status and future potential, Energy Environ. Sci. 17 (10) (2024) 3307–3328.

[40] S.K. Kuila, D.K. Gorai, S. Agarwal, R. Sarkar, C.S. Tiwary, T.K. Kundu, Gd3+ encapsulation on 2D-g-C3N4 nanostructure for spintronics and ultrasound assisted photocatalytic applications: first-principles and experimental studies, Small 20 (33) (2024) 2401670.

[41] X. Wang, Y. Li, R. Chu, Z. Zhang, W. Hou, L. Wang, L. Li, P. Zhang, Engineered an organic Z-scheme heterojunction of cu porphyrin-COF/g-C3N4 with planar covalent interaction for sustainable solar energy conversion, Chem. Eng. J. 16(13 (2025) 164922.

[42] C. Zhang, Y. Wang, W. Sun, Z. Hua, Z. Zhang, S. Gong, D. Wang, Y. Tian, Tailoring non-covalent interaction via single atom to boost interfacial charge transfer toward photoelectrochemical water oxidation, Adv. Mater. 37 (4) (2025) 2410632.

[43] X. Zhang, F. Wu, G. Li, L. Wang, J. Huang, A. Song, A. Meng, Z. Li, Dual electric field coupling with tunable schottky barrier synergistically regulating electronic configuration in CoP@Ni-CdS heterojunction for efficient photocatalytic H2 evolution, Adv. Funct. Mater. 35 (2) (2025) 2412527.

[44] X. Wu, Q. Yan, H. Wang, D. Wu, H. Zhou, H. Li, S. Yang, T. Ma, H. Zhang, Heterostructured catalytic materials as advanced electrocatalysts: classification, synthesis, characterization, and application, Adv. Funct. Mater. 34 (42) (2024) 2404535.

[45] W. Zhang, L. Yang, Z. Li, G. Nie, X. Cao, Z. Fang, X. Wang, S. Ramakrishna, Y. Long, L. Jiao, Regulating hydrogen/oxygen species adsorption via built-in electric fielddriven electron transfer behavior at the heterointerface for efficient water splitting, Angew. Chem. 136 (16) (2024) e202400888.

[46] X. Liang, X. Yang, J. Liu, L. Tu, W. Wei, H. Wang, M. Wu, L. Cai, Y. Zheng, Y. Chen, ROS-scavenging bioactive scaffold orchestrates bone regeneration for osteoporotic bone defect repair, Compos. Part B Eng. 281 (2024) 111528.

[47] D. Qin, C. Zhang, F. Qin, Y. Zhou, D. Huang, H. Wang, H. Luo, Q. Wang, L. Tang, W. Li, Cu single atoms mediated multiple active site reconfiguration to trigger Dual-pathway nonradical peroxymonosulfate activation process, Chem. Eng. J. 493 (2024) 152580.

[48] M. Kou, F. Qin, Y. Wang, L. Peng, Z. Hu, H. Zhao, Z. Zhang, Determination of singlet oxygen quantum yield based on the behavior of solvent dimethyl sulfoxide oxidation by singlet oxygen, Anal. Chim. Acta 1329 (2024) 343222.

[49] E.T.P. Ayala, F. Alves, I.S. e Carvalho, M. de Oliveira Souza, V.S. Bagnato, S. Pratavieira, Assessing reactive oxygen species generation during sonophotodynamic activity using chemical probes, Optical Methods for Tumor Treatment and Detection: Mechanisms and Techniques in Photodynamic Therapy,

884 23(19) (2024) 202435-202444.
885 [50] Y. Yao, Z. Sun, T. Li, Z. Zhao, Z. Li, X. Lu, Y. Wan, Y. Fan, Z. Chen, Advances in the
886 STructure–activity Relationship of Electrocatalytic C-N coupling: from
887 nanocatalysis to single metal site catalysis, ACS Nano 19 (20) (2025)
888 18947–18975.
889 [51] M. Li, J. Zhou, R. Di, Z. Zhang, X. Mu, X. Wang, Y. Gu, L. Su, J. Liu, C. Liu,
890 Piezoelectric potential activated interfacial electric field in BiFeO3@BaTiO3
891 heterojunction for rapid and round-the-clock photocatalytic degradation of organic
892 pollutants, J. Adv. Ceram. 13 (12) (2024) 2030–2042.
893 [52] X. Yang, Z. Guo, Y. Xu, Z. Li, Y. Zhou, Z. Yang, Z. Zhou, Y. Gao, J. Zhang, In situ
894 preparation and visible-light-driven photocatalytic degradation performance of
895 nano 3C-SiC@multilayer graphene oxide heterostructure, Chem. Res. Chin. Univ.
896 40 (3) (2024) 536–547.
897 [53] H. Wang, X. Zhou, J. Su, Z. Liu, B. Xiao, L. Yang, J. Wang, Y. Li, X. Lu, X. Zhu, Spinstate
898 regulation of heteronuclear Cu-Co dual-atomic sites via tuning electronic
899 asymmetry for enhanced oxygen reduction, Chem. Eng. J. 506 (2025) 160020.
900 [54] Q. Liu, Y. Lan, H. Shi, Y. Shi, Q. Pan, D. Yang, T. Wang, Cu–Ni bimetallic nanowires
901 with various structures originating from Ni reduction kinetics, Nano Lett. 24 (38)
902 (2024) 11992–11999.
903 [55] T. Shan, S. Ke, X. Yang, X. Yang, B. Weng, L. Shen, M.Q. Yang, Efficient hole
904 extraction to reactive oxidation sites over a Co3O4/Cs3Sb2Br9 pn heterojunction for
905 enhanced benzylic C(sp3)-H bond oxidation, Appl. Catal. B Environ. Energy 361

(2025) 124602.

[56] H. Phuoc Toan, D.-V. Nguyen, P.D.M. Phan, N. Hoai Anh, P.P. Ly, M.-T. Pham, S. H. Hur, T.D.T. Ung, D.D. Bich, M.C. Nguyen, Simultaneously utilizing excited holes and electrons for piezoelectric-enhanced photoproduction of H2O2 from S-scheme 2D S-Doped VO x/g-C3N4 nanostructures, ACS Appl. Mater. Interfaces 16 (22) (2024) 29421–29438.

[57] H. Li, F. Qi, J. Xiong, G. Pan, X. Gao, J. Chen, T. Ye, J. Zan, W. Xiong, C. Lin, Vacancy elimination enables scaffold with amplified photo-thermal-electric effect to promote osteoblast differentiation, Mater. Today Chem. 47 (2025) 102807.

[58] Z. Li, Q. Yu, X. Cui, Y. Wang, R. Xu, R. Lu, J. Chen, X. Zhou, C. Zhang, L. Li, Exosomes from young plasma stimulate the osteogenic differentiation and prevent osteoporosis via miR-142-5p, Bioact. Mater. 49 (2025) 502–514.

[59] F. Wei, M. Hughes, M. Omer, C. Ngo, A.S. Pugazhendhi, E. Kolanthai, M. Aceto, Y. Ghattas, M. Razavi, T.J. Kean, A multifunctional therapeutic strategy using P7C3 as a countermeasure against bone loss and fragility in an ovariectomized rat model of postmenopausal osteoporosis, Adv. Sci. 11 (21) (2024) 2308698.

[60] S. Zhu, W. Chen, A. Masson, Y.P. Li, Cell signaling and transcriptional regulation of osteoblast lineage commitment, differentiation, bone formation, and homeostasis, Cell Discov. 10 (1) (2024) 71.

[61] L. Wang, M. Ruan, Q. Bu, C. Zhao, Signaling pathways driving MSC osteogenesis: mechanisms, regulation, and translational applications, Int. J. Mol. Sci. 26 (3) (2025) 1311.

928 [62] S. Li, X. Cai, J. Guo, X. Li, W. Li, Y. Liu, M. Qi, Cell communication and relevant
929 signaling pathways in osteogenesis-angiogenesis coupling, Bone Res. 13 (1) (2025)
930 45.
931 [63] Q. Han, F. Wang, Electroacupuncture at GB20 improves cognitive ability and
932 synaptic plasticity via the CaM-CaMKII-CREB signaling pathway following cerebral
933 ischemia–reperfusion injury in rats, Acupunct. Med. 42 (1) (2024) 23–31.
934 [64] M. Wu, S. Wu, W. Chen, Y.-P. Li, The roles and regulatory mechanisms of TGF-β
935 and BMP signaling in bone and cartilage